Chemical Engineering Science 300 (2024) 120588

Contents lists available at ScienceDirect

Chemical Engineering Science

journal homepage: www.elsevier.com/locate/ces

Effect of physicochemical properties on critical sinking and attachment of respirable coal mine dust impacting on a water surface

Shihua Han [a], Mohammad Rezaee [a,*], Pedram Roghanchi [b]

[a] John and Willie Leone Family Department of Energy and Mineral Engineering, College of Earth and Mineral Sciences, The Pennsylvania State University, University Park, PA 16802, USA
[b] Department of Mining Engineering, College of Engineering, University of Kentucky, Lexington, KY 40506, USA

ARTICLE INFO

Keywords:
Respirable coal mine dust
Water surface
Contact angle
Surface tension
Critical velocity
Attachment efficiency

ABSTRACT

Respirable coal mine dust (RCMD) inhalation is identified as the main cause of the resurgence of coal worker's pneumoconiosis (CWP) since the mid-1990s. At present, the predominant dust control technology is the water spray system. However, in practice, the capture efficiency of RCMD by this technology is relatively low. To understand the capturing mechanism and develop improvement strategies, this research is focused on the surface chemistry study of RCMD and its impact on a water surface using a dynamic model. Proximate analysis, chemical, and mineral composition of a run-of-mine (ROM) coal sample from Appalachian region were analyzed using a proximate analyzer, Inductively Coupled Plasma Mass Spectrometry (ICP-MS), and X-ray Diffraction (XRD), respectively. Contact angles were measured by capillary rise test using the Washburn equation. Based on the dynamic model, the effects of particle size, density, contact angle, and surface tension on the critical sinking were investigated. It was pointed out in this work that reducing surface tension, in turn, decreases contact angle, which has been neglected in the literature. Regime maps for different minerals were created and showed that organic matter has the highest critical velocity due to its low density and high contact angle. Reducing water surface tension to the critical solid surface tension of coal around 30 mN/m could maximize the attachment efficiency. Scaling laws, constructed by force balance, led to the criteria of critical sinking: $U_{cr} \sim \sqrt{\frac{6(1-\cos\theta)}{(2D+1)}}\sqrt{\frac{\gamma_{lv}}{\rho_l R}}$, i.e., $We_{cr} \sim \frac{12(1-\cos\theta)}{(2D+1)}$. A semi-empirical formula for critical velocity was obtained by fitting the simulation data, $U_{cr} = 1.09\sqrt{\frac{6(1-\cos\theta)}{(2D+1)}}\sqrt{\frac{\gamma_{lv}}{\rho_l R}}$. Attachment efficiency was defined and formulated as $P_a = \frac{U_0^2}{U_{cr}^2} = \frac{We_0}{We_{cr}}$, establishing relationships between attachment efficiency and the physicochemical properties of RCMD and water droplets.

1. Introduction

The study of the interaction between solids and liquid–gas interfaces has many applications, such as water entry of projectiles (Aristoff and Bush, 2009; Truscott et al., 2014), locomotion of water walkers (Bush and Hu, 2006; Vella and Metcalfe, 2007) and bionic water strider robots (Yang et al., 2016), coal and mineral froth flotation (Nguyen, 2002), below-cloud scavenging (McDonald, 1963; Pemberton, 1960), and wet scrubbing (Wang et al., 2015). In addition, it is also relevant to dust suppression by water sprays as understanding the interaction between dust particles and droplets is very important in improving the dust capture efficiency (Zhou and Qin, 2021).

Respirable coal mine dust (RCMD) is generally referred to as coal dust particles with an aerodynamic diameter of less than 10 μm (Shekarian et al., 2021). Long-term overexposure to RCMD can cause coal worker's pneumoconiosis (CWP), also known as black lung (Shekarian et al., 2023). To further improve mine safety and health, the permissible exposure limit for RCMD enacted by the Mine Safety and Health Administration (MSHA) in the US was lowered from 2 mg/m^3 in 1972 (Federal Coal Mine Health and Safety Act of 1969) to 1.5 mg/m^3 in 2016 (79 Federal Register 24814) (NIOSH, 2021; Xu et al., 2018). However, meeting the established criteria using the current dust suppression technologies (e.g., water spray systems) is challenging (Zhou and Qin, 2021).

The capturing process of RCMD particles by water spray droplets can be considered as two steps: collision and attachment. The collision between RCMD particles and water droplets can occur under different mechanisms, such as inertia, interception, Brownian motion, and electrostatic attraction (Li et al., 2021). After the collision, RCMD particles

* Corresponding author.
E-mail address: m.rezaee@psu.edu (M. Rezaee).

https://doi.org/10.1016/j.ces.2024.120588
Received 26 April 2024; Received in revised form 23 July 2024; Accepted 30 July 2024
Available online 2 August 2024

Nomenclature

C	geometric factor of packed powders, m^5
d	particle diameter, m
d_{50}	particle diameter below which 50 % of particles are reported, m
F	force, N
g	gravitational acceleration, m/s^2
h	distance to the horizontal surface, m
H	distance of TPC line to the horizontal surface, m
k	coefficient for critical velocity
$\widehat{k}$	unit vector of y axis
m	mass of liquid in packed powders, kg
M	particle mass, kg
$\widehat{n}$	unit surface normal vector
p	pressure, Pa
P	circumference of the TPC line, m
R	particle radius, m
S	distance of the particle centroid to the horizontal surface, m
$\dot{S}$	particle velocity, m/s
$\ddot{S}$	particle acceleration, m/s^2
t	time, s
U	particle velocity, m/s
U_{cr}	critical particle velocity, m/s

Dimensionless numbers

Bo	Bond number
Ca	Capillary number
D	density ratio
Re	Reynolds number
We	Weber number
We_{cr}	critical Weber number

Greek letters

β	TPC angle, degree
γ	surface tension, N/m
θ	contact angle, degree
μ	viscosity of liquid, Pa·s
ρ_l	liquid density, kg/m^3
ϕ	angle between surface tension and the horizontal axis, degree
φ	velocity potential around a sphere, m^2/s
ρ_p	particle density, kg/m^3

Subscript

0	initial
a	air
am	additional mass
b	buoyancy
cr	critical
fd	form drag
g	gravity
l	liquid
lv	liquid–vapor
p	particle
P	pressure
s	surface
sl	solid–liquid
sv	solid–vapor
t	total

Accent

·	derivative with respect to time
··	second derivative with respect to time
ˆ	vector

Abbreviations

CWP	coal worker's pneumoconiosis
ICP-MS	Inductively Coupled Plasma Mass Spectrometry
LTA	low temperature ashing
MSHA	Mine Safety and Health Administration
NIOSH	National Institute for Occupational Safety and Health
ODE	ordinary differential equation
ROM	run-of-mine
RCMD	respirable coal mine dust
TPC	three-phase-contact
WPF	Whole Pattern Fitting
XRD	X-ray Diffraction

may immerse into the droplets, stay on the interface, or rebound to the air (Lee and Kim, 2008). Capture efficiency is the product of collision efficiency and attachment efficiency. The collision efficiency due to various mechanisms has been extensively investigated in aerosol science (Wang et al., 2010), while the attachment efficiency has been assumed to be unity (Davenport and Peters, 1978). However, the attachment efficiency depends on the surface chemistry of RCMD particles and water droplets. Hydrophobic particles, for example, may rebound from the surface of water droplets, resulting in an attachment efficiency of less than 1. Besides, the evaporation of droplets may cause the particles on the surface to be pushed away and become airborne again (Ladino et al., 2011). Therefore, sinking is the most appealing attachment scenario among the three modes (Mohal, 1988).

In practice, the water droplet size is usually much greater than that of RCMD particles (Colinet et al., 2010). The attachment of an RCMD particle to a water droplet can be, therefore, treated as the impact of an RCMD particle on a water surface (Wang et al., 2015). Only a few experimental studies (Ji et al., 2017; Wang et al., 2017; Xie et al., 2022) have been conducted on the impact of a micron-size particle on a liquid surface due to the challenges of monitoring and manipulating such a particle. Lee and Kim (2008) developed a dynamic model based on a potential flow theory and the Young-Laplace equation, and created a regime map of sinking, bouncing, and oscillating regions. The different regions were divided by the boundaries of critical velocities in the form of $\mathrm{WeBo}^{3/2} \sim D^2$, where We is the Weber number $\mathrm{We} = \rho_l U^2 d/\gamma$, Bo is the Bond number $\mathrm{Bo} = \rho_l g R^2/\gamma$, and D is the density ratio $D = \rho_p/\rho_l$. When a particle is entering the liquid surface against surface tension, the critical velocity of the particle to immerse is $U_{cr} = (1-\cos\theta)\sqrt{3\gamma_{lv}/(2R\rho_p)}$ (Kaptay, 2001; Vreeling et al., 2000), i.e., $\mathrm{We_{cr}} = 3(1-\cos\theta)^2/D$. When surface tension, fluid force, and other forces are considered, more complicated criteria for the critical sinking of micron-size particles have been reported (Ji et al., 2019; Kaptay, 2001).

It is known that the surface chemistry of RCMD and water droplets would affect the capture efficiency (Li et al., 2021; Xu et al., 2018; Zhou and Qin, 2021). Nevertheless, the intricate interplay among particle size, density, contact angle, and surface tension and their collective impact on capture efficiency remain incompletely elucidated, though the effects of those properties on particle critical velocities have been investigated. For example, it should be noted that changing surface tension will also influence contact angle according to Young's equation, $\cos\theta = (\gamma_{sv} - \gamma_{sl})/\gamma_{lv}$. Varying surface tension while keeping the contact angle constant as in the previous literature would underestimate the

effect of surface tension on the critical velocity.

This study explores the characteristics and surface chemistry of RCMD, including chemical and mineral composition and contact angle, and their effect on RCMD capturing efficiency. Based on a dynamic model, the effects of particle size, density, contact angle, and surface tension on the critical velocity were investigated. Regime maps for different minerals in RCMD were compared, and strategies for improving the capture efficiency of RCMD were developed accordingly. Finally, a semi-empirical critical velocity as a function of particle and liquid properties was developed and recommended to be used to determine the attachment efficiency.

2. Material and methods

2.1. Characteristics and surface chemistry of RCMD

A run-of-mine (ROM) coal sample was collected from an underground room and pillar operation, mining a thin sub-bituminous coal seam in the Appalachian region. To generate fresh RCMD for analysis, the sample was first crushed by jaw and roll crushers, and then ground by a Holmes pulverizer with a 60 mesh size sieve. The size analysis of the ground sample was performed using a Mastersizer with isopropanol as the dispersant. The suspension of coal particles was sonicated for 10 min before measurement. The ultrasound inside Mastersizer was in the pre-measurement mode and turned on for 10 s before size measurement. The measurement duration was 10 s, and the sample was measured 5 times. The particle size of the sample ground by Holmes pulverizer reached d_{50} of 13.9 μm (see Fig. S1 in Supplemental Information). The ground product from the pulverizer was then comprehensively characterized and the characteristics were incorporated into the dynamic model.

2.1.1. Proximate analysis

Standard method ASTM D5142 was conducted on a proximate analyzer for the automated measurement of ash yield, fixed carbon, moisture, and volatile matter. The moisture content was determined at 106 °C. The volatile matter was measured at 950 °C in an oxygen-free environment, followed by measuring the ash content (20.75 %) at 950 °C in an oxygen environment. The fixed carbon content (59.86 %) was measured indirectly, calculated by difference in terms of moisture, volatile matter, and ash. Table 1 shows the result of the proximate analysis of the ROM coal.

2.1.2. Chemical composition

The ash obtained from the proximate analysis was used to determine major elemental content through Inductively Coupled Plasma Mass Spectrometry (ICP-MS) analysis. A 0.2 g ash sample was digested by aqua regia (1 HNO_3 : 3 HCl) and concentrated hydrofluoric acid (HF), according to the ASTM D6357 method. The digested sample was diluted by the factors of 1 K and 20 K before ICP-MS analysis. Table 2 shows the inorganic chemical composition as oxide forms on a whole-coal basis. The total content of the inorganic elements is 18.42 %, which is close to the ash content of 20.75 % in the proximate analysis in Table 1.

2.1.3. Mineral composition

The mineral composition of the ROM coal sample was obtained by X-ray Diffraction (XRD) over a 2Theta range of 5° to 70° with Cu K_α radiation. Organic matter in the coal forms a broad bump at 2Theta of around 25° in XRD patterns. To reduce or remove the adverse effects of organic matter in the phase identification and quantification process, the ground sample was subjected to low-temperature ashing (LTA) in a plasma asher before the XRD scan. After about 19 h, 42.91 % of the initial sample was ashed. The XRD patterns of both the ROM and ashed coal samples are displayed in Fig. 1.

In Fig. 1, the peaks of mineral phases of the ashed ROM coal are intensified since some of the amorphous matter was removed during the ashing process. To quantify the mineral phases, the internal standard method was used, i.e., adding a certain amount of an internal standard to test samples. Zincite (ZnO) at 10 % by weight was added to both non-ashed and ashed ground samples, which were scanned on a rotating sample holder to obtain the XRD patterns. The quantification process was performed on Jade 8.6 by Whole Pattern Fitting (WPF). The mineral matter mainly contained kaolinite, quartz, pyrite, and muscovite. The quantification result of the coal sample is presented in Table 3.

Table 1
Proximate analysis of the ROM coal.

Component	Moisture	Volatile matter	Fixed carbon	Ash	Total
Content (%)	1.21	18.19	59.86	20.75	100.01

2.1.4. Contact angle

The capillary rise/liquid penetration method was employed to determine the contact angle of the ground sample. Four alkanes, that is, hexane, heptane, octane, and decane, were chosen as the reference liquids. For each liquid, the testing was repeated three times. The following procedure for the capillary rise test was performed. The bottom end of a glass tube (inner and outer diameters of 4 and 6 mm, respectively, thickness of 1 mm, height of around 8 cm) was sealed with cellulose filter paper using silicon glue. The sample (0.4000 ± 0.0010 g) was inserted into the glass tube and tapped 100 times to pack at a height of $1\frac{5}{8}$ inches. The bottom end of the glass tube was immersed into the alkane, and the weight loss, due to the liquid capillary rise, was recorded by a camera. The weight recording started when the reading of the balance became stable and started to decrease continuously. The Washburn equation (Eq. (1)) was used to measure the contact angle (Alghunaim et al., 2016; Washburn, 1921),

$$m^2 = \frac{C\rho_l^2\gamma_{lv}cos\theta}{\mu}t \tag{1}$$

where m denotes the mass of the liquid in the packed sample with a geometric factor of C, ρ_l signifies the density of the liquid, γ_{lv} represents the surface tension of the liquid, θ stands for the contact angle, and μ pertains to the viscosity of the liquid.

According to the Washburn equation, the square of weight loss (m^2) vs time (t) is linear. The weight loss due to liquid evaporation was considered and deducted in the calculation. The slope of the plot of m^2 vs t was calculated from the tests, and thus, the geometric factor was calculated from reference liquids, assuming that the reference liquids completely wet the sample ($\theta = 0$). After obtaining the geometric factor, the contact angle of water on the sample was calculated from the Washburn equation. The calculated contact angles of water on coal by different reference liquids were 87°±4° at the 95 % confidence level.

2.2. Dynamic model

Given that the ratio of water spray droplet size to RCMD particle size is significantly greater than 1, the collision between the particle and droplet can be treated as the impact of the particle on a horizontal water surface, as illustrated in Fig. 2.

The motion of the particle is governed by Newton's second law (Eq. (2)),

$$M\frac{d^2S}{dt^2} = F_t \tag{2}$$

where M, the mass of the particle, is calculated by Eq. (3), S represents the distance from the particle centroid to the horizontal surface, t stands for time, F_t denotes the total forces acting on the particle, and R and ρ_p correspond to the radius and density of the particle, respectively.

Table 2
Inorganic chemical composition of the ROM coal.

Component	Na_2O	MgO	Al_2O_3	SiO_2	K_2O	TiO_2	Fe_2O_3	CuO	ZnO	Total
Content (%)	0.51	0.18	5.96	3.02	0.77	0.30	7.11	0.19	0.37	18.42

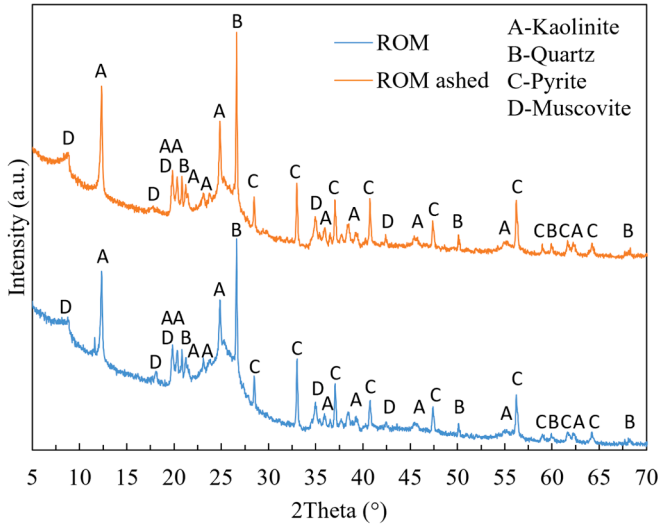

Fig. 1. XRD patterns of the ROM coal and the ashed ROM coal.

Table 3
Mineral composition of the ROM coal.

Component	Kaolinite	Quartz	Pyrite	Muscovite	Amorphous
Content (%)	13.33	2.22	2.56	3.78	78.22

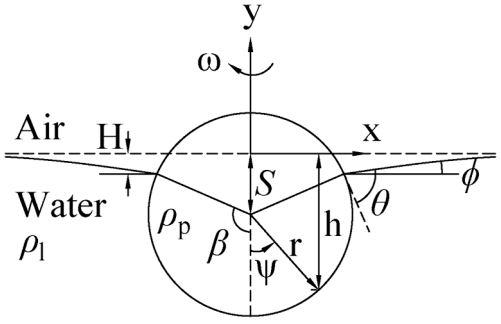

Fig. 2. Schematic diagram of the impact of a hydrophilic particle on a water surface.

$$M = \frac{4}{3}\pi R^3 \rho_p \tag{3}$$

F_t consists of gravity F_g, surface tension force F_s, and pressure force F_P, including buoyancy F_b, form drag F_{fd}, and added mass force F_{am}.

$$F_t = F_g + F_s + F_b + F_{fd} + F_{am} \tag{4}$$

Gravity F_g is given by Eq. (5), where g represents the acceleration due to gravity:

$$F_g = Mg = -\frac{4}{3}\pi R^3 \rho_p g \tag{5}$$

For surface tension force, only its vertical component affects the sinking of the particle, and is calculated as:

$$F_s = (\gamma_{lv} P)\sin\phi = \gamma_{lv}(2\pi R\sin\beta)\sin\phi \tag{6}$$

Here, P is the circumference of the three-phase-contact (TPC) line, γ_{lv} represents the surface tension of water, ϕ is the angle between surface tension and the horizontal axis, and β is the TPC angle.

Based on the geometry in Fig. 2,

$$\theta - \phi + \beta = 180^o \tag{7}$$

where θ is the contact angle. Therefore, surface tension in Eq. (6) can be written as

$$F_s = -2\pi R\gamma_{lv}\sin\beta\sin(\theta+\beta) \tag{8}$$

Based on the relative velocity between RCMD and water droplets, the Reynolds number falls within the order of 10–100. Therefore, the flow around an RCMD particle impacting on a water surface is assumed to be potential flow. The extended unsteady Bernoulli equation could be used to derive the pressure force of a particle impacting on a water surface (Fig. 2), as follows (Lee and Kim, 2008; Maranzoni, 2020):

$$\frac{\partial\varphi}{\partial t} + \frac{p}{\rho_l} + \frac{1}{2}|\nabla\varphi|^2 + gh = F(t) \tag{9}$$

The velocity potential φ around a sphere, expressed in spherical coordinate (r, ψ, ω) is given by:

$$\varphi = \frac{\dot{S}R^3\cos\psi}{2r^2} \tag{10}$$

In the context of the sphere's acceleration or deceleration, r and ψ are functions of time, and the relationships are (Paterson, 1983):

$$\begin{cases} \dot{r} = \dot{S}\cos\psi \\ r\dot{\psi} = -\dot{S}\sin\psi \end{cases} \tag{11}$$

At $r = R$ and $\psi = \beta$, $p = p_a - \rho_l gH$, and $h = H$, substituting Eqs. (10) and (11) into Eq. (9) gives (see Eqs. (S1)–(S3) in Supplemental Information):

$$\begin{aligned} F(t) &= \frac{R}{2}\ddot{S}\cos\beta - \dot{S}^2\cos^2\beta + \frac{\dot{S}^2}{2}\sin^2\beta + \frac{p_a - \rho_l gH}{\rho_l} + \frac{1}{2}\left(\dot{S}^2\cos^2\beta + \frac{\dot{S}^2\sin^2\beta}{4}\right) + gH \\ &= \frac{R}{2}\ddot{S}\cos\beta + \frac{p_a}{\rho_l} - \frac{9}{8}\dot{S}^2\cos^2\beta + \frac{5}{8}\dot{S}^2 \end{aligned} \tag{12}$$

Thus, Eq. (9) becomes:

$$\frac{\partial\varphi}{\partial t} + \frac{p}{\rho_l} + \frac{1}{2}|\nabla\varphi|^2 + gh = \frac{R}{2}\ddot{S}\cos\beta + \frac{p_a}{\rho_l} - \frac{9}{8}\dot{S}^2\cos^2\beta + \frac{5}{8}\dot{S}^2 \tag{13}$$

On the surface of the sphere,

$$\ddot{S}\left(\frac{R\cos\psi}{2}\right) + \frac{p}{\rho_l} - \frac{9}{8}\dot{S}^2\cos^2\psi + \frac{5}{8}\dot{S}^2 + gh = \frac{R}{2}\ddot{S}\cos\beta + \frac{p_a}{\rho_l} - \frac{9}{8}\dot{S}^2\cos^2\beta + \frac{5}{8}\dot{S}^2 \tag{14}$$

Solving the above Eq. (14) for p yields:

$$p(R,\psi) = p_a - \rho_l gh + \frac{\rho_l R}{2}\ddot{S}(\cos\beta - \cos\psi) + \frac{9\rho_l}{8}\dot{S}^2(\cos^2\psi - \cos^2\beta) \tag{15}$$

Therefore, the vertical component of the pressure force acting on the sphere is calculated by:

$$F_P = \int (p - p_a)(-\hat{n} \bullet \hat{k}) dS = \int (p - p_a)\cos\psi dS = \frac{\pi}{3}R^2\rho_l g\left(3S\cos^2\beta - 2R\cos^3\beta - 3S + 2R\right) - \frac{\pi}{6}R^3\rho_l\ddot{S}\left(\cos^3\beta - 3\cos\beta + 2\right) + \frac{9\pi}{16}R^2\rho_l\dot{S}^2\sin^4\beta \quad (16)$$

In Eq. (16), the first term of the expression represents buoyancy, the second term corresponds to the added mass force, and the third term accounts for the form drag:

$$F_b = \frac{\pi}{3}R^2\rho_l g\left(3S\cos^2\beta - 2R\cos^3\beta - 3S + 2R\right) \quad (17)$$

$$F_{fd} = \frac{9\pi}{16}R^2\rho_l\dot{S}^2\sin^4\beta = -\frac{9\pi}{16}R^2\rho_l\frac{dS}{dt}\left|\frac{dS}{dt}\right|\sin^4\beta \quad (18)$$

$$F_{am} = -\frac{\pi}{6}R^3\rho_l\left(\cos^3\beta - 3\cos\beta + 2\right)\frac{d^2S}{dt^2} \quad (19)$$

For Eq. (17), the generalized Archimedes' principle (Keller, 1998; Mansfield et al., 1997) states that the buoyancy equals the weight of the volume of water, which includes the volume of the spherical cap and vertical cylinder (Liu et al., 2009) in Fig. 2, displaced by the sphere particle. Regarding Eq. (19), the added mass of a sphere is equal to one-half of the liquid mass displaced by the submerged sphere (Brennen, 1982; Limacher et al., 2018; Pantaleone and Messer, 2011).

Substituting Eqs. (5), (8), (17), (18), and (19) into Eq. (2) yields:

$$M\frac{d^2S}{dt^2} = -\frac{4}{3}\pi R^3\rho_p g - 2\pi R\gamma_{lv}\sin\beta\sin(\theta+\beta) + \frac{\pi}{3}R^2\rho_l g\left(3S\cos^2\beta - 2R\cos^3\beta - 3S + 2R\right) - \frac{9\pi}{16}R^2\rho_l\frac{dS}{dt}\left|\frac{dS}{dt}\right|\sin^4\beta - \frac{\pi}{6}R^3\rho_l\left(\cos^3\beta - 3\cos\beta + 2\right)\frac{d^2S}{dt^2} \quad (20)$$

In the above Eq. (20), there are two unknowns, S and β. According to the geometry in Fig. 2, the following relationship is established between S and β:

$$S = H + R\cos\beta \quad (21)$$

where H can be derived from the Young-Laplace equation and expressed as (James, 1974; Lo, 1983; Nguyen, 2002)

$$H = R\sin\beta\sin(\theta+\beta)\left(\ln\left(\frac{4}{\sqrt{Bo}\left(\sin\beta - \sin\beta\cos(\beta+\theta)\right)}\right) - 0.57721\right) \quad (22)$$

Eq. (22) can be simplified to (Wang et al., 2015):

$$H = R\sin\beta\sin(\theta+\beta)\left(\ln\left(\frac{2.5}{\sqrt{Bo}}\right) - 0.57721\right) \quad (23)$$

Substituting Eq. (23) into Eq. (21) results in:

$$H = R\sin\beta\sin(\theta+\beta)\left(\ln\left(\frac{2.5}{\sqrt{Bo}}\right) - 0.57721\right) + R\cos\beta \quad (24)$$

Therefore, the system of two equations with two unknowns, S and β, as given in Eqs. (20) and (24), can be succinctly expressed as:

$$\begin{cases} M\frac{d^2S}{dt^2} = F_t\left(\frac{d^2S}{dt^2}, \frac{dS}{dt}, S, \beta\right) \\ S = Z(\beta) + R\cos\beta \end{cases} \quad (25)$$

This system encompasses a nonlinear 2nd-order ordinary differential equation (ODE). The numerical solution of Eq. (25) was performed using the Python function solve_ivp in SciPy library. The initial conditions at time $t = 0$ were set as $S(0) = R$, $U(0) = -U_0$, and $\beta(0) = 0$. For a given particle size, varying the initial particle velocity when numerically solving Eq. (25) results in different particle trajectories S. The particle's impact modes can be categorizes based on the value of S as follows: i) $S < -r$, sink; ii) $-r \le S \le r$, oscillate; iii) $S > r$, rebound. Repeating this process for different particle sizes can generate a regime map depicting particle velocity versus particle size. This map illustrates distinct regions corresponding to sinking, oscillating, and rebounding impact modes.

Similar regime maps can be developed by varying other characteristics of particles, such as particle density, surface tension, and contact angle. By systematically adjusting these parameters and obtaining the critical velocities, comprehensive regime maps could be created to provide insights into how different factors influence the sinking, oscillating, and rebounding behaviors of particles. This approach allows for a thorough understanding of the system's dynamics and provides insights into predicting the particle's impact modes under various conditions.

2.2.1. Validation

The validation of the dynamic model proved challenging due to the complexities of observing the impact of a single RCMD particle on a water surface using high-speed video cameras. Consequently, existing experimental data from the literature were employed for validation purposes. Table 4 outlines the properties of particles used in the validation process. The density and surface tension of water are 1000 kg/m^3 and 72.8 mN/m, respectively. The comparison of the experimental data with the simulation results, particularly in various impact modes, is shown in Fig. 3. Fig. 4 illustrates the critical velocity distinguishing sinking and oscillating regions. The comparison demonstrates the capability of the dynamic model to accurately predict the particle trajectory upon impact on a water surface and effectively determine the critical velocity delimiting sinking and oscillating regions.

2.2.2. Simulation

The dynamic model was employed to investigate the effects of particle size, density, contact angle, and liquid surface tension on the critical sinking velocity of RCMD impacting on a water surface. Particles smaller than 1 μm were excluded from this study due to variations in capturing mechanisms, such as Brownian diffusion, which are not considered in the dynamic model (Park et al., 2005). The contact angle between RCMD and water/air interface was determined as 87° using the capillary rise method in Section 2.1.4. The RCMD characterization in Section 2.1 revealed the presence of minerals, such as kaolinite, quartz, pyrite, and muscovite, in RCMD particles. Carbonate minerals (mainly calcite) has been also reported in RCMD, sourcing from coal or rock dusting (Colinet and Listak, 2012; Johann-Essex et al., 2017). Therefore,

Table 4
Parameters of particles used for validation.

Impact mode	Particle diameter (μm)	Particle density (kg/m^3)	Initial velocity (m/s)	contact angle (°)	Reference
Sinking	150	1180	2.65	115	(Ji et al., 2017)
Rebounding	1920	1320	0.89	154	(Lee and Kim, 2008)
Oscillating	154	1180	2.21	115	(Ji et al., 2017)
Sinking/ Oscillating	50–200	1180	U_0	126	(Wang et al., 2017)

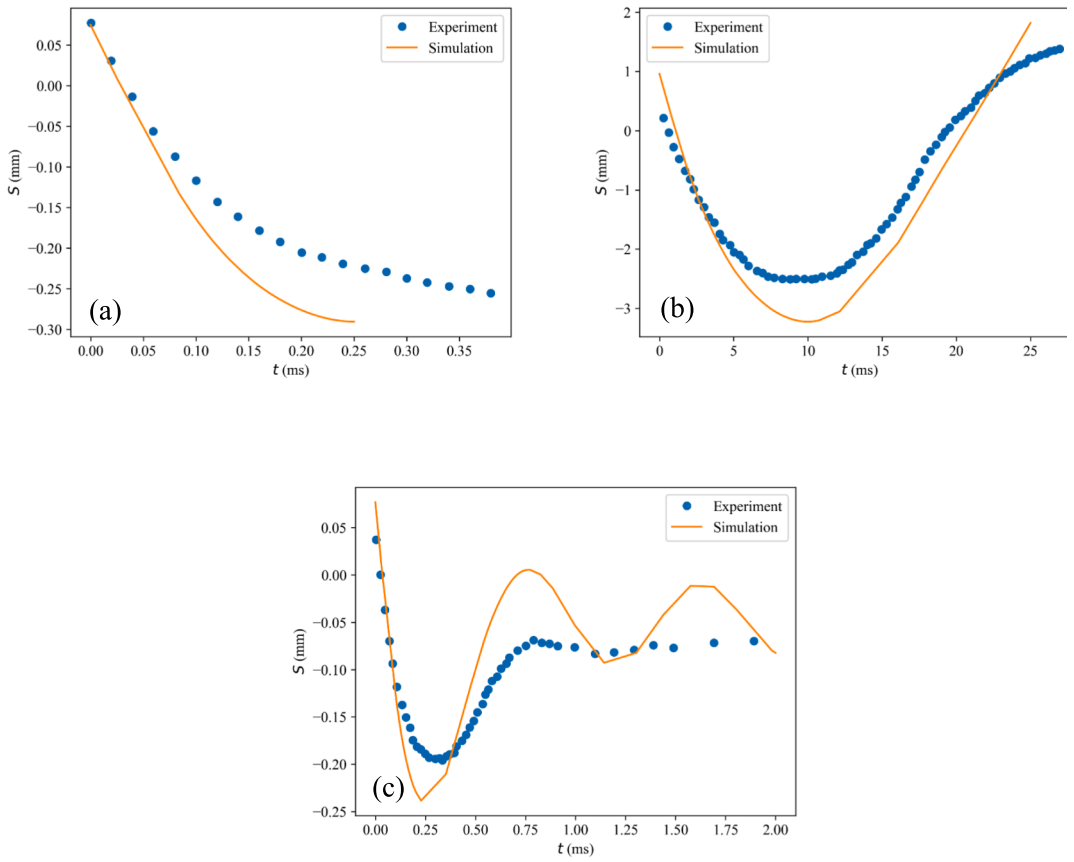

Fig. 3. Comparison of experimental data and simulation results depicting displacement in different impact modes: (a) sinking, (b) rebounding, and (c) oscillating.

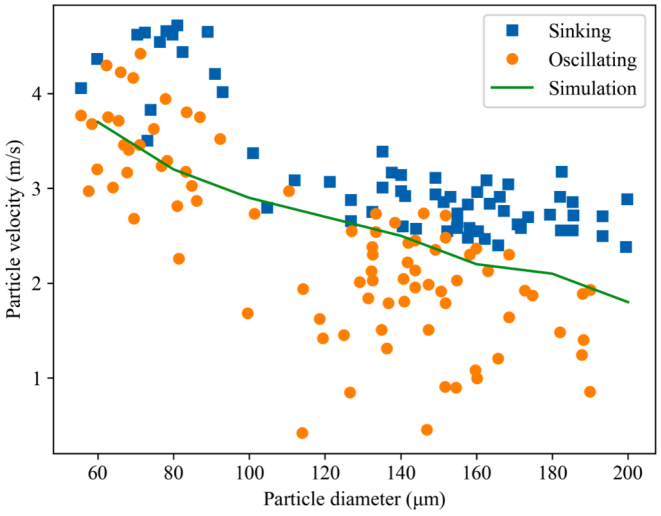

Fig. 4. Comparison of experimental data (Wang et al., 2017) with simulation results of critical velocity.

the critical sinking of those minerals was also investigated in this work, with properties listed in Table 5. The contact angles of those minerals were sourced from the literature.

2.3. Relationship between surface tension and contact angle

The effect of surface tension on the critical velocity is intricate since decreasing surface tension also reduces contact angle. Young's equation describes the relationship between contact angle and surface tension as follows:

$$\cos\theta = \frac{\gamma_{sv} - \gamma_{sl}}{\gamma_{lv}} \tag{26}$$

However, the lack of γ_{sv} and γ_{sl} data inhibits the calculation of the contact angle from Eq. (26). To address this limitation, an equation of state was developed by Neumann et al. (1974), which facilitates the calculation of solid surface tension γ_{sv} from a pair of liquid surface tension and the corresponding contact angle. The equations governing this calculation are as follows:

$$cos\theta = \frac{(0.015\gamma_{sv} - 2)\sqrt{\gamma_{lv}\gamma_{sv}} + \gamma_{lv}}{\gamma_{lv}\left(0.015\sqrt{\gamma_{lv}\gamma_{sv}} - 1\right)} \tag{27}$$

$$\gamma_{sl} = \frac{\left(\sqrt{\gamma_{lv}} - \sqrt{\gamma_{sv}}\right)^2}{1 - 0.015\sqrt{\gamma_{lv}\gamma_{sv}}} \tag{28}$$

Using the data provided in Table 5 for water surface tension and contact angle, along with Eq. (27), we can calculate the surface tensions of coal and minerals as presented in Table 6, presumed to be constant. By substituting the calculated solid surface tension γ_{sv} into Eq. (28) or cross-referencing the conversion tables for liquid surface tensions to contact angles (Neumann et al., 1980), the relationship between liquid surface tension and contact angle can be established. The relevant data for coal is presented in Table 7.

3. Results and discussion

3.1. Regime maps for RCMD

3.1.1. Effect of particle size and density

The regime map of particle velocity versus particle size is illustrated in Fig. 5a, showing the distinct regions of sinking and oscillating. The

Table 5
Properties of particles and liquid used in simulation.

Particle	Particle diameter (μm)	Particle density (kg/m^3)	Initial velocity (m/s)	Liquid density (kg/m^3)	Liquid surface tension (mN/m)	Contact angle (°)	Reference
Coal	1–10	1300	U_0	1000	72.8	87	Current work
Kaolinite		2600				20	(Shang et al., 2010; Xi et al., 2020)
Quartz		2650				26	(Deng et al., 2018; Janczuk and Zdziennicka, 1994; Luo et al., 2015; Xie et al., 2021)
Pyrite		5000				60	(Cheng et al., 2020; Raichur et al., 2000; Xu et al., 2020)
Muscovite		2850				10	(Jiang et al., 2019; Xue et al., 2018; Zhang et al., 2022)
Calcite		2710				45	(Huang et al., 2023; Jiao et al., 2023; Rahimi et al., 2017; Wu et al., 1996)

Table 6
Calculated solid surface tensions of different minerals.

Mineral	Coal	Kaolinite	Quartz	Pyrite	Muscovite	Calcite
Solid surface tension γ_{sv} (mN/m)	31.07	68.88	66.35	47.51	71.91	56.31

Table 7
Relationship between liquid surface tension and contact angle of coal.

Liquid surface tension (mN/m)	72.8	60	50	40	32
Contact angle (°)	87	71	58	41	14

parameters of the coal particle and liquid used in the simulation are listed in Table 5. In Fig. 5a, in the region above the delineated line, the particle will sink into the water, while in the region below the line, the particle will oscillate and float on the interface. The velocity that separates the two regions is called critical velocity, U_{cr}. Notably, as the particle diameter decreases, the critical velocity increases significantly, which implies that it is more difficult for smaller particles to sink into water. Therefore, the critical velocity can serve as an indicator for attachment efficiency, with higher critical velocity corresponding to lower attachment efficiency, and vice versa.

The regime map of particle velocity versus particle density (Fig. 5b) shows that the critical velocity decreases as the particle density increases. In other words, high-density particles sink into water more efficiently. Conversely, low-density particles have lower attachment efficiency as they require higher critical velocity. In Table 5, we can see that coal has a very small density, while other minerals have higher densities. Table 1 and Table 3 show that about 80 % of coal is organic matter and the remaining 20 % is other minerals. This means that organic matter is the most difficult material to capture from the perspective of density.

3.1.2. Effect of contact angle

The effect of contact angle on the critical velocity is presented in Fig. 6. Contact angle is an indicator of wettability, with a higher contact angle indicating lower wettability and vice versa. This is consistent with the relationship between contact angle and critical velocity presented in Fig. 6. As the contact angle decreases, the particle becomes more hydrophilic and wettable, and the critical velocity decreases. In contrast, an increase in contact angle signifies a more hydrophobic particle, leading to the increase in critical velocity. Notably, when the contact angle is greater than 100° (Fig. 6), the particle could bounce back from the interface. Therefore, to improve the capture efficiency, minimizing the contact angle is crucial, indicating a more hydrophilic particle. As highlighted in Table 5, coal has the largest contact angle among the components, suggesting that organic matter presents the greatest challenge for capture due to its hydrophobic nature.

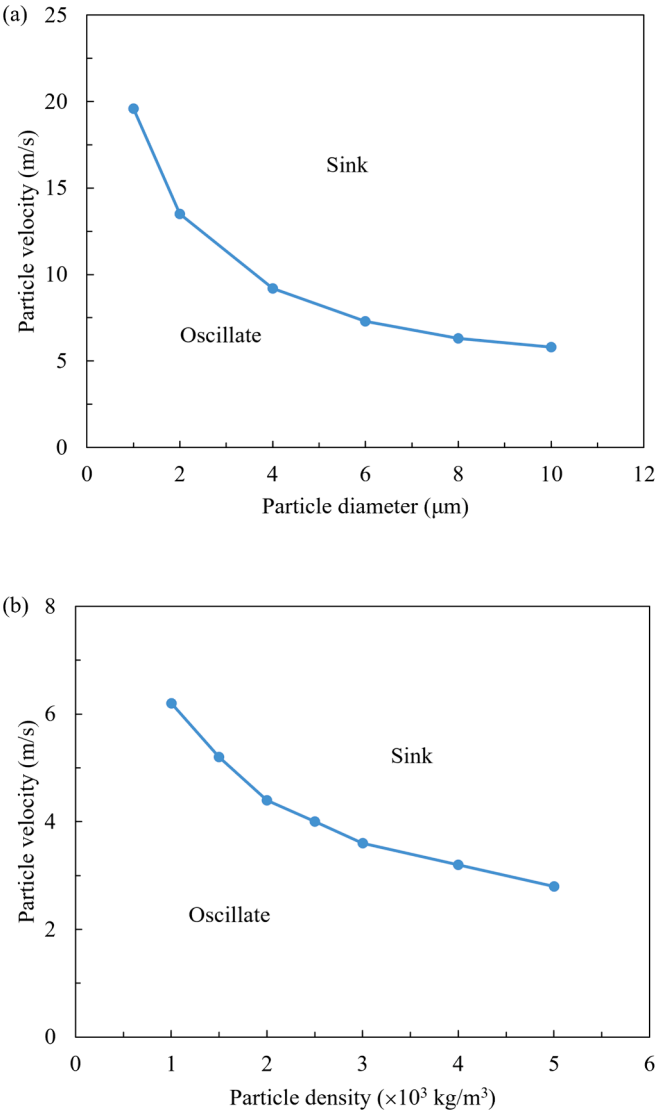

Fig. 5. Effects of (a) particle size and (b) density (d = 10 μm) on the critical velocity.

3.1.3. Effect of surface tension

The effect of surface tension on the critical velocity is displayed in Fig. 7. Additionally, this figure includes the calculated critical velocity while altering the surface tension but maintaining the contact angle constant, providing a basis for comparison. It is evident that these two critical lines diverge as the surface tension decreases. This clearly indicates that the significance of the contact angle impact on the critical

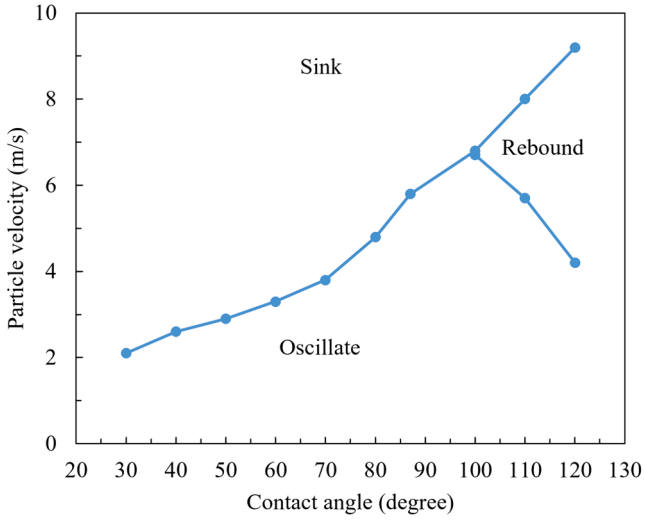

Fig. 6. Effect of contact angle on the critical velocity (d = 10 μm).

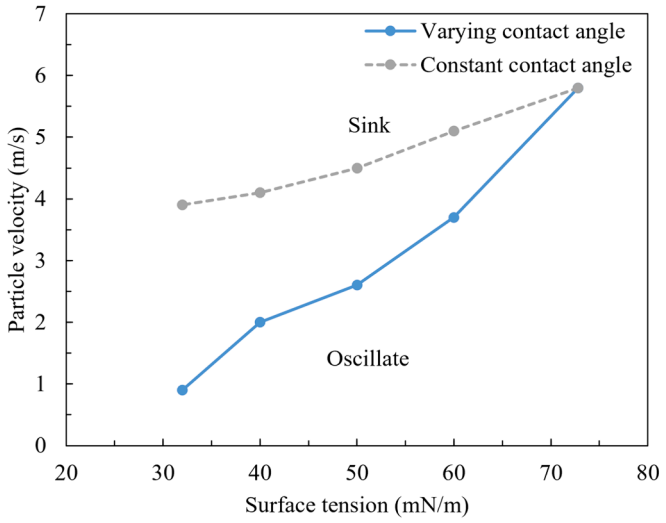

Fig. 7. Effect of surface tension on the critical velocity (d = 10 μm).

velocity and attachment efficiency. Table 7 shows that there is a decrease in contact angle as the surface tension decreases. The combined effect of the reduced surface tension and the resulting decrease in contact angle synergistically leads to a significant reduction in critical velocity. Therefore, reducing liquid surface tension emerges as a pivotal and effective method to enhance capture efficiency.

3.1.4. *Regime maps for different minerals of RCMD*

The regime maps for different minerals in coal, identified by XRD analysis (Fig. 1), are plotted in Fig. 8. A notable observation is that the critical velocities of different minerals are much smaller than that of coal. When establishing a hierarchy based on critical velocities, the order of capture difficulty is as follows: coal ≫ pyrite ≈ calcite > quartz ≈ kaolinite > muscovite. Therefore, the parameters of the water spray system should be designed with an emphasis on the capture of organic matter instead of mineral matter in coal mine applications.

The calculated solid surface tensions for different dust components, with coal having the lowest value, are listed in Table 6. According to Eq. (26), when the surface tension of the liquid is reduced to the solid surface tension, i.e., $\gamma_{lv} = \gamma_{sv}$, the contact angle becomes 0, resulting in complete wetting of the solid by the liquid. Given that the surface tensions of water and coal are 72.8 and 31.07 mN/m, respectively, reducing

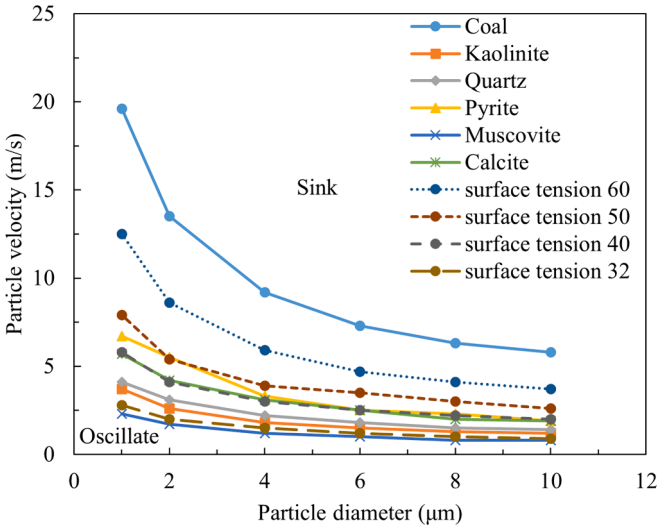

Fig. 8. Regime maps for different minerals and coal at different liquid surface tensions (dashed lines).

the surface tension in the water spray system to around 30 mN/m could achieve the maximum attachment efficiency. This critical surface tension is consistent with the values reported in the literature (Kilau, 1990; Parekh and Aplan, 1978; Wang, 1991). The regime maps for coal at different liquid surface tensions (Fig. 8) highlight a significant reduction in critical velocities of coal when the surface tension is lowered to 32 mN/m. This confirms that reducing surface tension is an effective method for enhancing attachment efficiency.

3.2. *Scaling laws for critical velocity*

Fig. 8 exhibits a similarity in critical velocity regardless of various properties of the particle. Scaling laws constructed by the force balance are employed to derive the critical velocity as a function of particle size, density, contact angle, and surface tension. The force analysis of RCMD impacting a water surface at its critical velocity is presented in Fig. 9 and Fig. 10. The results revealed that gravity and buoyancy are negligible forces, while the surface tension and drag force are the predominant forces. This observation is further supported by the dimensionless numbers in this study: Bond number Bo $< 10^{-5}$, Reynolds number Re in

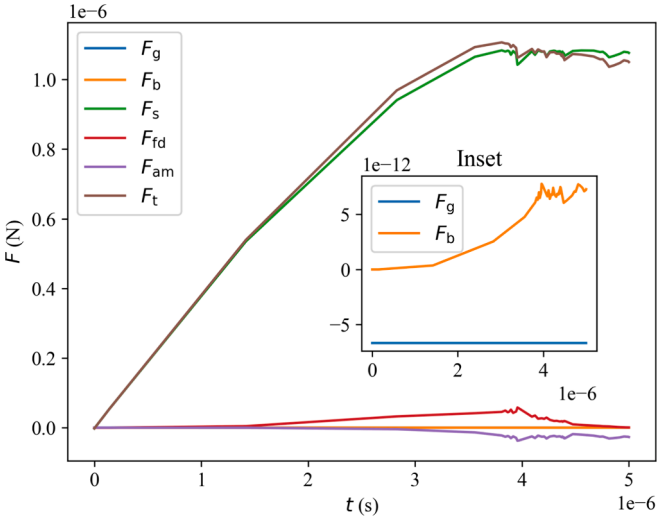

Fig. 9. Force analysis of RCMD (d = 10 μm) at the critical sinking velocity U_0 = 5.8m/s.

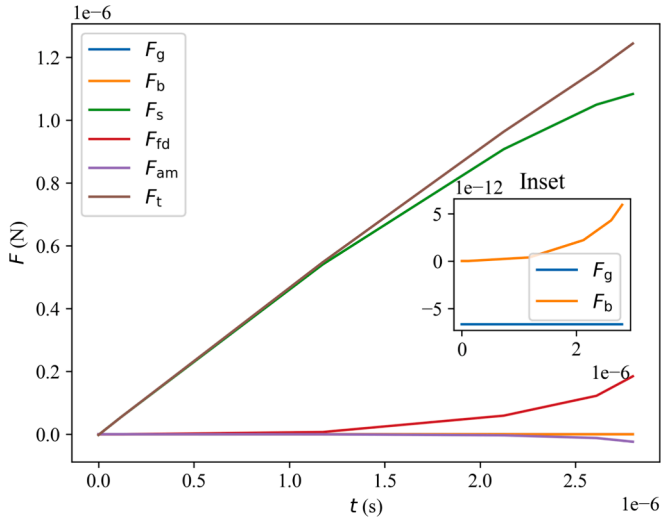

Fig. 10. Force analysis of RCMD (d = 10 μm) at the sinking velocity U_0 = 7m/s.

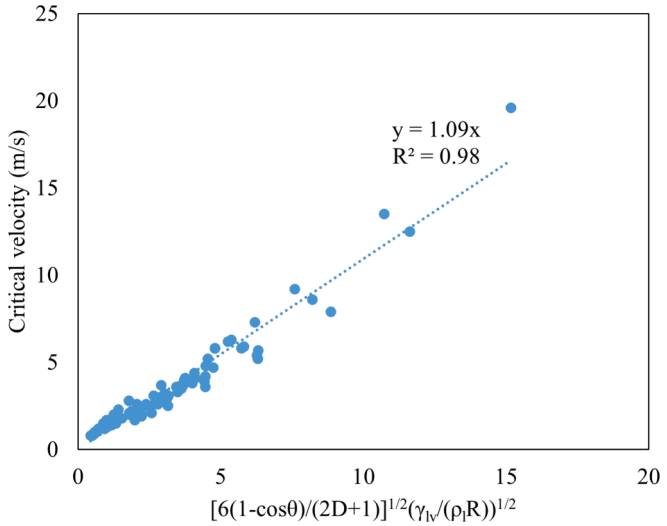

Fig. 11. Critical velocity as a function of particle size, density, contact angle, and surface tension.

the range of 20–70, Weber number We < 7, and Capillary number Ca < 0.25. Therefore, Eq. (20) can be simplified as:

$$M\frac{\mathrm{d}^2S}{\mathrm{d}t^2} \sim -2\pi R\gamma_{lv}\sin\beta\sin(\theta+\beta) - \frac{9\pi}{16}R^2\rho_l\frac{dS}{dt}\left|\frac{dS}{dt}\right|\sin^4\beta - \frac{\pi}{6}R^3\rho_l(\cos^3\beta - 3\cos\beta + 2)\frac{d^2S}{dt^2} \tag{29}$$

The added mass force reaches maximum of $\frac{2\pi}{3}R^3\rho_l\frac{d^2S}{dt^2}$ when $\cos\beta = -1$. Because of the non-linearity of velocity in the expression of form drag and the dominance of surface tension, the effect of drag force is reflected through a subsequent correction parameter. Eq. (29) can be further simplified as:

$$\left(\frac{4}{3}\pi R^3\rho_p + \frac{2\pi}{3}R^3\rho_l\right)\frac{\mathrm{d}^2S}{\mathrm{d}t^2} \sim -\pi R\gamma_{lv}(\cos\theta - \cos(\theta+2\alpha)) \tag{30}$$

The surface tension force has a maximum value of $\pi R\gamma_{lv}(1-\cos\theta)$ (Chen et al., 2018). Therefore, the acceleration is in the following scale:

$$\frac{\mathrm{d}^2S}{\mathrm{d}t^2} \sim \frac{1.5\gamma_{lv}(1-\cos\theta)}{\rho_l R^2(2D+1)} \tag{31}$$

When the contact angle is less than 90°, at low Weber numbers, it is assumed that the depth of pinch-off is in the magnitude of d (Aristoff and Bush, 2009; Chen et al., 2019; Duez et al., 2007; Truscott et al., 2014), that is, $|\Delta S_{cr}| \sim d$. Therefore, the time scale of critical sinking is:

$$t_{cr} \sim \sqrt{\frac{|\Delta S_{cr}|}{\ddot{S}}} \sim \left(\frac{8(2D+1)}{3(1-\cos\theta)}\right)^{\frac{1}{2}}\left(\frac{\rho_l R^3}{\gamma_{lv}}\right)^{\frac{1}{2}}$$

Therefore, the critical velocity is obtained in the following scale,

$$U_{cr} \sim \ddot{S}t_{cr}\left(\frac{6(1-\cos\theta)}{(2D+1)}\right)^{\frac{1}{2}}\left(\frac{\gamma_{lv}}{\rho_l R}\right)^{\frac{1}{2}} \tag{32}$$

that is,

$$We_{cr} \sim \frac{12(1-\cos\theta)}{(2D+1)} \tag{33}$$

The simulation data in this work are plotted together in Fig. 11 according to the proportional relationship of Eq. (32). The linear line obtained from regression analysis fits well with the data, which proves the applicability of Eq. (32). Using the slope of the fitted line to include the effect of drag force results in the critical velocity as follows:

$$U_{cr} = k\left(\frac{6(1-\cos\theta)}{(2D+1)}\right)^{\frac{1}{2}}\left(\frac{\gamma_{lv}}{\rho_l R}\right)^{\frac{1}{2}} \tag{34}$$

where k = 1.09. Equation (34) suggests that (i) RCMD particles of smaller size, lower density, and larger contact angle need higher critical velocity to sink into water droplets, and (ii) reducing the water surface tension can decrease the critical velocity, enhancing the attachment efficiency and the total capture efficiency. This explains the mechanism behind the practice of adding surfactants to the water spray system to improve the capture efficiency, as surfactants can reduce the surface tension of water droplets and increase the attachment efficiency.

3.3. Attachment efficiency

The attachment efficiency can be defined as the ratio of the surface area submerged in the water to the surface area of the particle, that is,

$$P_a = \frac{2\pi R(R - R\cos\beta)}{4\pi R^2} = \frac{1-\cos\beta}{2} \tag{35}$$

For the contact angle less than 90°, we assume that there is no cavity and H (in Fig. 2) is close to 0. Therefore, the attachment efficiency can be written as:

$$P_a \approx \frac{|\Delta S|}{|\Delta S_{cr}|} = \frac{U_0^2}{U_{cr}^2} = \frac{\rho_l d U_0^2}{\gamma_{lv}}\frac{(2D+1)}{12k^2(1-\cos\theta)} = \frac{We_0}{We_{cr}} \tag{36}$$

In Eq. (36), the attachment efficiency increases with the particle size and density but decreases with the surface tension and contact angle. The maximum attachment efficiency can be achieved when the particle velocity is greater than the critical sinking velocity. Therefore, for a given particle, the attachment efficiency can be improved by reducing the

Table 8
Comparison of attachment efficiency for RCMD (U_0 = 5m/s) at different liquid surface tensions.

Particle size (μm)		1	2	4	6	8	10
Attachment efficiency (%)	γ_{lv} = 72.8mN/m	9	18	36	55	73	92
	γ_{lv} = 32mN/m	100	100	100	100	100	100

critical velocity via adjusting the water surface tension and contact angle. For example, the attachment efficiency for RCMD is maximized by reducing the water surface tension from 72.8 to 32 mN/m, as shown in Table 8. At the water surface tension of 72.8 mN/m, as the particle size decreases from 10 to 1 μm, the attachment efficiency drops from 92 % to only 9 %. When the surface tension is reduced to 32 mN/m, the attachment efficiencies for all the particles larger than 1 μm reach the maximum of 100 %.

In practice, surfactants are commonly added to water spray systems to improve the capture efficiency of RCMD. The attachment efficiency formula (Eq. (36)) quantitatively reveals how surfactants enhance capture efficiency by reducing surface tension and contact angle. To maximize attachment efficiency, the surface tension of liquid should be reduced to lower than the solid surface tension, which is approximately 30 mN/m for RCMD.

4. Conclusions

In this study, the relationship between the physicochemical properties of RCMD and attachment to water droplets was investigated. A dynamic model was employed to study the critical sinking of RCMD impacting a water droplet, represented by water surface as the droplet to particle size ratio is significantly higher than 1. Parametric studies revealed that the critical velocity increases with decreasing particle size and density and increasing contact angle, while it decreases as liquid surface tension is reduced. A lower critical velocity indicates RCMD particles more readily sink into water, resulting in higher attachment and capture efficiencies. Therefore, reducing liquid surface tension emerges as an essential and effective method for enhancing capture efficiency. Furthermore, this work highlighted that reducing surface tension also decreases contact angle as governed by Young's equation, which has been neglected in previous literature.

The regime maps for different minerals calculated by the dynamic model revealed that organic matter requires the highest critical velocity due to its low density and high contact angle. Reducing liquid surface tension to the coal critical solid surface tension of approximately 30 mN/m can achieve the maximum attachment efficiency.

Force analysis showed that gravity and buoyancy are negligible forces when RCMD particles impact a water surface, while surface tension and drag force serve as the major acting forces. Scaling laws derived from the force balance led to the formulation of the scale of critical velocity as $U_{\mathrm{cr}} \sim \left(\frac{6(1-\cos\theta)}{(2D+1)}\right)^{\frac{1}{2}}\left(\frac{\gamma_{lv}}{\rho_l R}\right)^{\frac{1}{2}}$, i.e., $\mathrm{We}_{\mathrm{cr}} \sim \frac{12(1-\cos\theta)}{(2D+1)}$. A semi-empirical formula for critical velocity was developed by fitting the simulation data, that is, $U_{cr} = k\left(\frac{6(1-\cos\theta)}{(2D+1)}\right)^{\frac{1}{2}}\left(\frac{\gamma_{lv}}{\rho_l R}\right)^{\frac{1}{2}}$, where $k = 1.09$. This critical velocity formula was further incorporated into the attachment efficiency equation, which was defined and expressed as $P_a = \frac{U_0^2}{U_{cr}^2} = \frac{\rho_l d U_0^2}{\gamma_{lv}} \frac{(2D+1)}{12k^2(1-\cos\theta)} = \frac{We_0}{We_{cr}}$. This formula effectively links attachment efficiency with the physicochemical properties of RCMD and water droplets, providing a valuable framework for devising strategies to improve RCMD capture efficiency in coal mines.

CRediT authorship contribution statement

Shihua Han: Writing – original draft, Visualization, Validation, Software, Methodology, Investigation, Formal analysis, Conceptualization. **Mohammad Rezaee:** Writing – review & editing, Validation, Supervision, Resources, Project administration, Methodology, Investigation, Funding acquisition, Formal analysis, Data curation, Conceptualization. **Pedram Roghanchi:** Writing – review & editing, Resources, Funding acquisition.

Declaration of competing interest

The authors declare the following financial interests/personal relationships which may be considered as potential competing interests: Mohammad Rezaee reports financial support was provided by National Institute for Occupational Safety and Health. If there are other authors, they declare that they have no known competing financial interests or personal relationships that could have appeared to influence the work reported in this paper.

Data availability

Data will be made available on request.

Acknowledgements

The authors gratefully acknowledge the financial support from the National Institute for Occupational Safety and Health (NIOSH) through contract # 75D30119C06390. Special thanks are extended to the coal companies which provided samples, as well as Penn State EMS Energy Institute (EI) and Material Research Institute (MRI) for their provision of analytical facilities. Shihua Han expresses gratitude to Dr. David Williams for his valuable discussions.

Appendix A. Supplementary data

Supplementary data to this article can be found online at https://doi.org/10.1016/j.ces.2024.120588.

References

Alghunaim, A., Kirdponpattara, S., Newby, B.-M.Z., 2016. Techniques for determining contact angle and wettability of powders. Powder Technol. 287, 201–215.
Aristoff, J.M., Bush, J.W.M., 2009. Water entry of small hydrophobic spheres. J. Fluid Mech. 619, 45–78.
Brennen, C., 1982. A Review of Added Mass and Fluid Inertial Forces. Naval Civil Engineering Laboratory, Sierra Madre, California.
Bush, J.W.M., Hu, D.L., 2006. Walking on Water: Biolocomotion at the Interface. Annu. Rev. Fluid Mech. 38, 339–369.
Chen, H., Liu, H.-R., Lu, X.-Y., Ding, H., 2018. Entrapping an impacting particle at a liquid–gas interface. J. Fluid Mech. 841, 1073–1084.
Chen, H., Liu, H.-R., Gao, P., Ding, H., 2019. Submersion of impacting spheres at low Bond and Weber numbers owing to a confined pool. J. Fluid Mech. 884.
Cheng, W., Deng, Z., Tong, X., Lu, T., 2020. Hydrophobic agglomeration of fine pyrite particles induced by flotation reagents. Minerals 10.
Colinet, J.F., Cecala, A.B., Chekan, G.J., Organiscak, J.A., Wolfe, A.L., 2010. Best practices for dust control in metal/nonmetal mining. In: U.S. Department of Health and Human Services, Centers for Disease Control and Prevention, National Institute for Occupational Safety and Health (Ed.). DHHS (NIOSH), Pittsburgh PA.
Colinet, J.F., Listak, J.M., 2012. Silica and respirable content in rock dust samples. Coal Age 117, 48–52.
Davenport, H.M., Peters, L.K., 1978. Field studies of atmospheric particulate concentration changes during precipitation. Atmos. Environ. 12, 997–1008.
Deng, Y., Xu, L., Lu, H., Wang, H., Shi, Y., 2018. Direct measurement of the contact angle of water droplet on quartz in a reservoir rock with atomic force microscopy. Chem. Eng. Sci. 177, 445–454.
Duez, C., Ybert, C., Clanet, C., Bocquet, L., 2007. Making a splash with water repellency. Nat. Phys. 3, 180–183.
Huang, Z., Kuang, J., Yu, M., Ding, D., 2023. Quinic acid as a novel depressant for efficient flotation separation of scheelite from calcite. Physicochem. Probl. Miner. Process.
James, D.F., 1974. The meniscus on the outside of a small circular cylinder. J. Fluid Mech. 63, 657–664.
Janczuk, B., Zdziennicka, A., 1994. A study on the components of surface free-energy of quartz from contact-angle measurements. J. Mater. Sci. 29, 3559–3564.
Ji, B., Song, Q., Yao, Q., 2017. Numerical study of hydrophobic micron particle's impaction on liquid surface. Phys. Fluids 29.
Ji, B., Song, Q., Wang, A., Yao, Q., 2019. Critical sinking of hydrophobic micron particles. Chem. Eng. Sci. 207, 17–29.
Jiang, H., Gao, Y., Khoso, S.A., Ji, W., Hu, Y., 2019. A new approach for characterization of hydrophobization mechanisms of surfactants on muscovite surface. Sep. Purif. Technol. 209, 936–945.
Jiao, F., Li, W., Wang, X., Yang, C., Zhang, Z., Fu, L., Qin, W., 2023. Application of EDTMPS as a novel calcite depressant in scheelite flotation. Int. J. Min. Sci. Technol. 33, 639–647.

Johann-Essex, V., Keles, C., Rezaee, M., Scaggs-Witte, M., Sarver, E., 2017. Respirable coal mine dust characteristics in samples collected in central and northern Appalachia. Int. J. Coal Geol. 182, 85–93.
Kaptay, G., 2001. Interfacial aspects to produce particulate reinforced metal matrix composites. In: Pandey, A.B., Kendig, K.L., Watson, T.J. (Eds.), TMS. TMS, Indianapolis, Indiana, pp. 71–99.
Keller, J.B., 1998. Surface tension force on a partly submerged body. Phys. Fluids 10, 3009–3010.
Kilau, H.W., 1990. Influence of Sulfate Ion on the Coal-Wetting Performance of Anionic Surfactants. US Department of the Interior, Bureau of Mines.
Ladino, L., Stetzer, O., Hattendorf, B., Günther, D., Croft, B., Lohmann, U., 2011. Experimental study of collection efficiencies between submicron aerosols and cloud droplets. J. Atmos. Sci. 68, 1853–1864.
Lee, D.G., Kim, H.Y., 2008. Impact of a superhydrophobic sphere onto water. Langmuir 24, 142–145.
Li, S., Zhao, B., Lin, H., Shuang, H., Kong, X., Yang, E., 2021. Review and prospects of surfactant-enhanced spray dust suppression: mechanisms and effectiveness. Process Saf. Environ. Prot. 154, 410–424.
Limacher, E., Morton, C., Wood, D., 2018. Generalized derivation of the added-mass and circulatory forces for viscous flows. Phys. Rev. Fluids 3.
Liu, X., Wang, X., Liang, Y., Zhou, F., 2009. Floating behavior of hydrophobic glass spheres. J. Colloid Interface Sci. 336, 743–749.
Lo, L.L., 1983. The meniscus on a needle – a lesson in matching. J. Fluid Mech. 132, 65–78.
Luo, B., Zhu, Y., Sun, C., Li, Y., Han, Y., 2015. Flotation and adsorption of a new collector α-Bromodecanoic acid on quartz surface. Miner. Eng. 77, 86–92.
Mansfield, E.H., Sepangi, H.R., Eastwood, E.A., 1997. Equilibrium and mutual attraction or repulsion of objects supported by surface tension. Philos. Trans. R. Soc. London Series A: Mathe. Phys. Eng. Sci. 355, 869–919.
Maranzoni, A., 2020. Galilean-invariant expression for Bernoulli's equation. J. Hydraul. Eng. 146.
McDonald, J.E., 1963. Rain washout of partially wettable insoluble particles. J. Geophys. Res. 68, 4993–5003.
Mohal, B.R., 1988. Enhancement of the Wettability of Coal Powders Using Surfactants. The Pennsylvania State University.
Neumann, A., Absolom, D., Francis, D., Oss Van, C., 1980. Conversion tables of contact angles to surface tensions. Sep. Purif. Methods 9, 69–163.
Neumann, A.W., Good, R.J., Hope, C.J., Sejpal, M., 1974. An equation-of-state approach to determine surface tensions of low-energy solids from contact angles. J. Colloid Interface Sci. 49, 291–304.
Nguyen, A.V., 2002. Empirical equations for meniscus depression by particle attachment. J. Colloid Interface Sci. 249, 147–151.
NIOSH, 2021. Best practices for dust control in coal mining, in: U.S. Department of Health and Human Services, Centers for Disease Control and Prevention, National Institute for Occupational Safety and Health (Ed.), second ed. DHHS (NIOSH), Pittsburgh, PA.
Pantaleone, J., Messer, J., 2011. The added mass of a spherical projectile. Am. J. Phys 79, 1202–1210.
Parekh, B., Aplan, F., 1978. The critical surface tension of wetting of coal. Rec. Devel. Sep. Sci. 4, 107–113.
Park, S.H., Jung, C.H., Jung, K.R., Lee, B.K., Lee, K.W., 2005. Wet scrubbing of polydisperse aerosols by freely falling droplets. J. Aerosol. Sci. 36, 1444–1458.
Paterson, A.R., 1983. A First Course in Fluid Dynamics. Cambridge University Press.
Pemberton, C.S., 1960. Scavenging action of rain on non-wettable particulate matter suspended in the atmosphere. Int. J. Air Pollut. 3, 168–178.
Rahimi, S., Irannajad, M., Mehdilo, A., 2017. Comparative studies of two cationic collectors in the flotation of pyrolusite and calcite. Int. J. Miner. Process. 167, 103–112.
Raichur, A.M., Wang, X.H., Parekh, B.K., 2000. Quantifying pyrite surface oxidation kinetics by contact angle measurements. Colloids Surf., A-Physicochem. Eng. Aspects 167, 245–251.
Shang, J., Flury, M., Harsh, J.B., Zollars, R.L., 2010. Contact angles of aluminosilicate clays as affected by relative humidity and exchangeable cations. Colloids Surf., A-Physicochem. Eng. Aspects 353, 1–9.
Shekarian, Y., Rahimi, E., Rezaee, M., Su, W.-C., Roghanchi, P., 2021. Respirable coal mine dust: a review of respiratory deposition, regulations, and characterization. Minerals 11, 696.
Shekarian, Y., Rahimi, E., Rezaee, M., Roghanchi, P., 2023. A systematic review of occupational exposure to respirable coal mine dust (RCMD) in the U.S. mining industry. Int. J. Coal Sci. Technol. 10.
Truscott, T.T., Epps, B.P., Belden, J., 2014. Water entry of projectiles. Annu. Rev. Fluid Mech. 46, 355–378.
Vella, D., Metcalfe, P.D., 2007. Surface tension dominated impact. Phys. Fluids 19, 072108.
Vreeling, J.A., Ocelik, V., Pei, Y.T., Van Agterveld, D.T.L., De Hosson, J.T.M., 2000. Laser melt injection in aluminum alloys: On the role of the oxide skin. Acta Mater. 48, 4225–4233.
Wang, A., Song, Q., Yao, Q., 2015. Behavior of hydrophobic micron particles impacting on droplet surface. Atmos. Environ. 115, 1–8.
Wang, A., Song, Q., Ji, B., Yao, Q., 2017. In-situ observation of hydrophobic micron particle impaction on liquid surface. Powder Technol. 311, 408–415.
Wang, X., Zhang, L., Moran, M.D., 2010. Uncertainty assessment of current size-resolved parameterizations for below-cloud particle scavenging by rain. Atmos. Chem. Phys. 10, 5685–5705.
Wang, X.-H., 1991. Pyrite surface characterization and control for advanced fine coal desulfurization technologies, United States, p. 52.
Washburn, E.W., 1921. The dynamics of capillary flow. Phys. Rev. 17, 273.
Wu, W., Giese, R.F., VanOss, C.J., 1996. Change in surface properties of solids caused by grinding. Powder Technol. 89, 129–132.
Xi, P., Ma, R., Liu, W., 2020. Research on the hydrophilicity of non-coal kaolinite and coal kaolinite from the viewpoint of experiments and DFT simulations. Symmetry 12.
Xie, J., Li, C., Yang, T., Fu, Z., Li, R., 2022. The motion behavior of micron fly-ash particles impacting on the liquid surface. ACS Omega 7, 29813–29822.
Xie, R., Zhu, Y., Liu, J., Li, Y., 2021. A self-assembly mixed collector system and the mechanism for the flotation separation of spodumene from feldspar and quartz. Miner. Eng. 171.
Xu, G., Chen, Y., Eksteen, J., Xu, J., 2018. Surfactant-aided coal dust suppression: A review of evaluation methods and influencing factors. Sci. Total Environ. 639, 1060–1076.
Xu, S., Cheng, D., Skinner, W., Brito e Abreu, S., 2020. Application of ToF-SIMS to predict contact angles of pyrite particles. Miner. Eng. 147.
Xue, X., Xu, Z., Pedruzzi, I., Li, P., Yu, J., 2018. Interaction between low molecular weight carboxylic acids and muscovite: Molecular dynamic simulation and experiment study. Colloids Surf., A Physicochem. Eng. Asp. 559, 8–17.
Yang, K., Liu, G., Yan, J., Wang, T., Zhang, X., Zhao, J., 2016. A water-walking robot mimicking the jumping abilities of water striders. Bioinspir. Biomim. 11, 066002.
Zhang, C., Wang, X., Li, L., Jin, J., Polson, R., Miller, J., 2022. Multiscale water drop contact angles at selected silica surfaces. Physicochem. Probl. Miner. Process.
Zhou, Q., Qin, B., 2021. Coal dust suppression based on water mediums: A review of technologies and influencing factors. Fuel 302, 121196.

Effect of Physicochemical Properties on Critical Sinking and Attachment of Respirable Coal Mine Dust Impacting on a Water Surface

Shihua Han[a], Mohammad Rezaee[a,*], Pedram Roghanchi[b]

[a] Department of Energy and Mineral Engineering, College of Earth and Mineral Sciences, The Pennsylvania State University, University Park, PA 16802, USA

[b] Department of Mining Engineering, College of Engineering, University of Kentucky, Lexington, KY 40506, USA

*Corresponding Author: m.rezaee@psu.edu

Supplemental Information

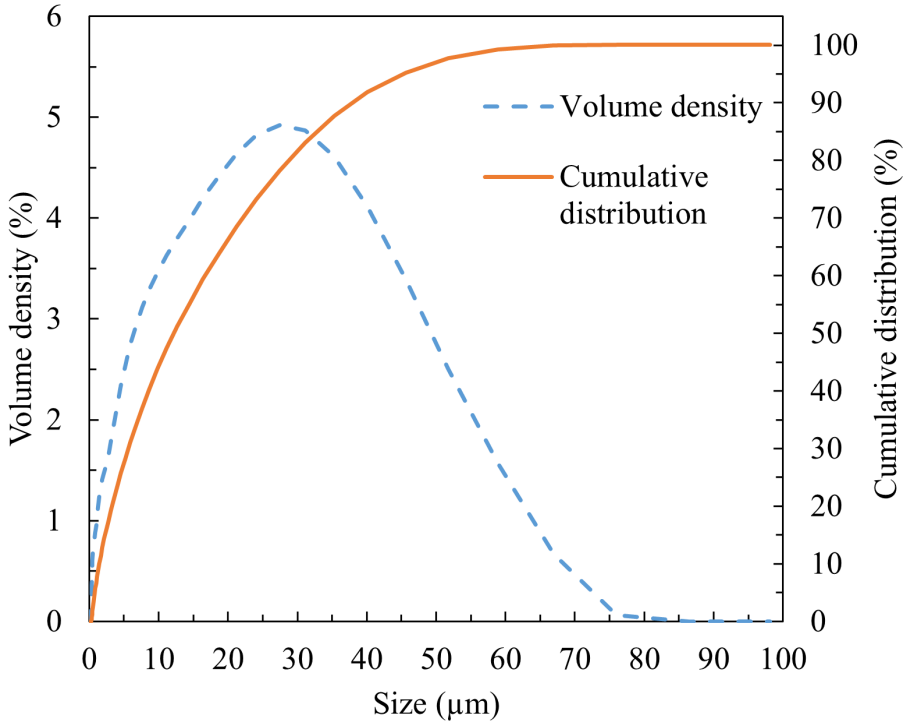

Figure S1 Particle size distribution of respirable coal mine dust

$$\frac{\partial \varphi}{\partial t} = \frac{\ddot{S}R^3 \cos\psi}{2r^2} - \frac{\dot{S}^2 R^3 \cos^2\psi}{r^3} + \frac{\dot{S}^2 R^3}{2r^3}\sin^2\psi \tag{S1}$$

$$\nabla\varphi = \frac{\partial \varphi}{\partial r}\hat{r} + \frac{1}{r}\frac{\partial \varphi}{\partial \psi}\hat{\psi} + \frac{1}{r\sin\psi}\frac{\partial \varphi}{\partial \omega}\hat{\omega} = -\frac{\dot{S}R^3 \cos\psi}{r^3}\hat{r} - \frac{\dot{S}R^3 \sin\psi}{2r^3}\hat{\psi} \tag{S2}$$

$$|\nabla\varphi|^2 = \left(-\frac{\dot{S}R^3 \cos\psi}{r^3}\right)^2 + \left(-\frac{\dot{S}R^3 \sin\psi}{2r^3}\right)^2 \tag{S3}$$